

A fast full-wave solver for trans-abdominal high-intensity focused ultrasound treatment planning

S. R. Haqshenas^{1,2}, P. G lat¹, E. van 't Wout³, T. Betcke², N. Saffari¹

1 Department of Mechanical Engineering, University College London, London, WC1E 7JE, UK

2 Department of Mathematics, University College London, London, WC1H 0AY, UK

3 Institute for Mathematical and Computational Engineering, Pontificia Universidad Cat lica de Chile, Santiago, Chile

E-mail: s.haqshenas@ucl.ac.uk

Abstract.

High-intensity focused ultrasound (HIFU) is a promising treatment modality for the non-invasive ablation of pathogenic tissue in many organs. Optimal treatment planning strategies based on high-performance computing methods are expected to form a vital component of a successful clinical outcome in which healthy tissue is preserved and accurate focusing achieved. The practical application of the algorithms informing these strategies depends on the ability to produce fast and accurate full-wave patient-specific simulations, with minimal computational overheads. For realistic clinical scenarios, all simulation methods which employ volumetric meshes require several hours or days to run on a computer cluster. The boundary element method (BEM) is an effective approach for modelling the wave field because only the boundaries of the hard and soft tissue regions require discretisation. A multiple-domain BEM formulation with a novel preconditioner for solving the Helmholtz transmission problem (HTP) is presented in this paper. Numerical experiments are performed to solve HTP in multiple domains comprising: i) human ribs, an abdominal fat layer and liver tissue, ii) a human kidney and a perinephric fat layer, exposed to the acoustic field generated by a HIFU array transducer. The time required to solve the equations associated with these problems on a single workstation is of the order of minutes. These results demonstrate the great potential of this new BEM formulation for rapid and accurate HIFU treatment planning.

1. Introduction

Surgical and ablative techniques are the most effective local therapies for solid malignancies (Cranston, 2015). The significant side effects associated with surgical

interventions have led to an ongoing quest for safer, more efficient and better tolerated alternatives. In recent years, there has been a notable shift away from open surgery towards less invasive procedures such as laparoscopic and robotic surgery, and from there to other methods for *in situ* tumour destruction, often involving energy based destruction. These include embolization (Waked et al., 2017), radiofrequency (Crocetti, 2018), microwave (Meloni et al., 2017) and laser ablation (Sartori et al., 2017), cryoablation (Werner et al., 2018) and high-intensity focused ultrasound (HIFU) (ter Haar, 2007). HIFU is a procedure which uses high-intensity ultrasound to thermally ablate a localised region of tissue. For abdominal applications, the ultrasound is typically generated by a focused transducer located extracorporeally.

HIFU treatment planning may be defined as obtaining a solution to a mathematical inverse problem whose output provides a patient specific and clinically suitable means of thermally ablating a volume of diseased tissue, whilst keeping the energy absorption in healthy tissue below an ablative threshold. There is growing clinical consensus that, for an optimal outcome, the planning phase must be achieved prior to the intervention, using numerical simulations on anatomical data obtained from patient scans. Optimal excitation protocols of a multi-element transducer may then be determined (Gélat et al., 2012), thus ensuring that diseased tissue is accurately ablated. Indeed, the treatment of abdominal tumours presents challenges due to soft tissue heterogeneity and the presence of strong scatterers, such as bone and the bowel. In HIFU ablation of tumours of the liver, ribs both scatter and absorb ultrasound, which may lead not only to an aberration of the focus but can also cause skin burns (Casper et al., 2010, Gélat et al., 2014, Ramaekers et al., 2017).

The most promising full-wave computationally efficient 3D numerical method for HIFU treatment planning of transcostal tumours is currently the boundary element method (BEM) (van 't Wout et al., 2015, Betcke et al., 2017). In BEM, the partial differential equation that models the wave propagation is essentially reformulated into a boundary integral equation defined on the interfaces. The boundary solutions and potential integrals are used to calculate the field at any point in the domain. Being based on Green's function representations, BEM is almost devoid of the numerical dispersion and dissipation effects commonly associated with numerical schemes such as k -space pseudospectral and finite-difference time domain methods (Marburg, 2018, Robertson et al., 2014). For sound-hard scatterers, issues of long computing times have been overcome through analytical preconditioners used in conjunction with hierarchical matrix (\mathcal{H} -matrix) compression techniques (Betcke et al., 2017).

In order for such schemes to be incorporated into a clinically-relevant treatment planning framework, it is vital that they be extended to include the ability to deal with some degree of tissue heterogeneity. Whilst soft tissue such as skin, muscle and fat have similar compressional wave speeds and densities (Duck, 2013), fat attenuates ultrasound energy significantly and causes beam aberration at the focus. This impedes focal heating during HIFU treatment of renal cancer, due to the presence of perinephric fat (Ritchie et al., 2013, Cranston, 2015, Suomi et al., 2018). It also remains to be established to which extent ultrasound can penetrate rib bone and how important it is to account for this phenomenon when modelling the propagation of ultrasound in the abdominal region. The ability to model the propagation of ultrasound through ribs and

assess the importance of this relative to the case of locally reacting ribs (Gélat et al., 2014) would be beneficial, particularly when studying the heat transfer mechanisms which lead to skin burns in HIFU patients (Ramaekers et al., 2017). There is therefore a requirement for resorting to multi-domain BEM to deal with the treatment planning complexities outlined above.

A number of multi-domain acoustic BEM formulations have been proposed (Cheng et al., 1991, Medeiros et al., 2014, Huang and Liu, 2016). In these approaches, the boundary integral equation (BIE) was applied to each domain. Due to the matrices resulting from domain discretisation being fully populated, the set-up time and memory consumption scale quadratically with respect to the number of degrees of freedom (Brunner et al., 2010). Fast BEM schemes have been introduced for the Helmholtz equation, resulting in a quasilinear complexity. The merits of such methods, namely the fast multipole method and hierarchical matrices, were discussed by Brunner *et al.* (Brunner et al., 2010) where a scattering problem involving a 22 m long, 2 m thick cylinder immersed in water was analyzed for excitation frequencies up to 200 Hz. Such fast BEM schemes have been applied to multi-domain Helmholtz problems. A fast multipole BEM method for 3D multi-domain acoustic scattering problems was described by Wu et al (Wu et al., 2012).

The above studies investigate cases where the ka (where k is the wavenumber and a is the characteristic size of the domain) is substantially less than that encountered in HIFU applications. Determining which BEM scheme is optimal for solving multi-domain Helmholtz problems at frequencies relevant to HIFU problems remains an active area of research. Previously, a fast BEM model was developed to solve the scattering from a single and perfectly rigid domain (van 't Wout et al., 2015, Betcke et al., 2017). In this paper, we present a fast multiple domain BEM model to compute both the scattered and transmitted ultrasonic fields in soft-tissue and bone. This formulation employs advanced preconditioning and \mathcal{H} -matrix compression techniques which enable the wave equation to be solved in large domain sizes relative to the wavelengths involved. The equations were implemented and solved using the open source library Bempp (Śmigaj, Betcke, Arridge, Phillips and Schweiger, 2015). The simulations were validated against analytical solutions, where available. Subsequently, the scattered field was calculated for the following computational domains: i) a layer of abdominal fat, human ribs and liver tissue, and ii) a human kidney model and a perinephric fat layer. In both scenarios, the incident field is generated by a spherical section array transducer operating at the frequency of 1 MHz. Finally, the suitability and limitations of this BEM scheme for use in HIFU treatment planning are discussed.

2. Model formulation

In this paper, we consider the problem of solving acoustic wave propagation in a medium made of the exterior domain Ω^0 and non-overlapping domains Ω^j , $j = 1, \dots, n$ with different physical properties, i.e. density and wave speed. A single trace formulation which involves one Dirichlet data and one Neumann data at each point of each interface is used and implemented. As a result, this formulation holds true where only two domains are in contact with each other, thus not allowing for triple points.

2.1. Wave equation

It is well known that the propagation of ultrasonic waves in tissue at amplitudes relevant to HIFU is nonlinear, where nonlinearities are mainly confined to the focal region of the field (Yuldashev et al., 2013). Crucial information pertaining to treatment planning of cancers of the abdomen can however be obtained via linear models. Suomi et al (Suomi et al., 2018) report substantial focal splitting when planning treatment for cancers of the kidney, where acoustic full-wave simulations on a domain size of $200 \times 200 \times 200 \text{ mm}^3$ using a k -space pseudospectral method required approximately two days to complete on a 400 core cluster. Compensating for beam aberrations is likely to involve techniques employing a full matrix capture of the transducer array, thus necessitating as many forward simulations as there are elements of the array (typically 256, 512 or 1024). The forward calculations may then be incorporated into a constrained optimisation scheme (Gélat et al., 2012, 2014) so that field quantities are kept below a specified threshold. Fast linear full-wave modelling schemes applied to heterogeneous media therefore have a distinct advantage in compensating for soft tissue and bone heterogeneities. The first phase of a treatment plan can be envisaged as consisting of a purely linear computation to calculate the optimal array excitation vector for sparing healthy tissue. This excitation vector can then serve as input data into a nonlinear model confined to the focal region so that precise thermal dose metrics may be more accurately determined.

The linear full-wave propagation is modelled by the Helmholtz system as follows

$$\left\{ \begin{array}{ll} \Delta p^j(\mathbf{x}) + k_j^2 p^j(\mathbf{x}) = 0, & \text{for } \mathbf{x} \in \Omega^j \\ \Delta p_s(\mathbf{x}) + k_0^2 p_s(\mathbf{x}) = 0, & \text{for } \mathbf{x} \in \Omega^0 \\ \gamma_D^{j,+}(p_s(\mathbf{x}) + p_{\text{inc}}(\mathbf{x})) = \gamma_D^{j,-} p^j(\mathbf{x}), & \text{for } \mathbf{x} \in \partial\Omega^j \\ \frac{1}{\rho_0} \gamma_N^{j,+}(p_s(\mathbf{x}) + p_{\text{inc}}(\mathbf{x})) = \frac{1}{\rho_j} \gamma_N^{j,-} p^j(\mathbf{x}), & \text{for } \mathbf{x} \in \partial\Omega^j \\ \lim_{|\mathbf{x}| \rightarrow \infty} |\mathbf{x}| \left(\nabla p_s(\mathbf{x}) \cdot \frac{\mathbf{x}}{|\mathbf{x}|} - ik_0 p_s(\mathbf{x}) \right) = 0. & \end{array} \right. \quad (1)$$

where k_j , ρ_j , $\gamma_D^{j,\pm}$ and $\gamma_N^{j,\pm}$ are the wavenumber, the mass density, and the Dirichlet and Neumann traces associated with the domain j for $j = 1, \dots, n$ taken from the exterior(+)/interior(-), respectively. The wavenumber k_j is complex with the positive real part equals to $2\pi/\lambda$ where λ is the wavelength in meters, and the positive imaginary part being $\alpha_0 f^b$ where α_0 is the attenuation coefficient in Neper $\text{m}^{-1} \text{Hz}^{-1}$, f is the frequency in Hz and b is the exponent. This frequency power law model is used to account for the attenuation of wave propagation in soft and hard tissues (Hamilton et al., 1998). The traces are defined as follows:

$$\left\{ \begin{array}{l} \gamma_D^{j,\pm} p(\mathbf{x}) := \lim_{\Omega^\pm \ni \mathbf{x}' \rightarrow \mathbf{x}} p(\mathbf{x}') \\ \gamma_N^{j,\pm} p(\mathbf{x}) := \lim_{\Omega^\pm \ni \mathbf{x}' \rightarrow \mathbf{x}} \nabla p(\mathbf{x}') \cdot \mathbf{n}^j(\mathbf{x}') \end{array} \right. \quad (2)$$

where $\mathbf{n}^j(\mathbf{x})$ is the normal vector on the boundary $\partial\Omega^j$ and points outwards to the exterior of domain Ω^j (for both $\gamma_N^{j,\pm}$ traces), see Fig. 1. Here, $p_s(\mathbf{x})$, $p_{\text{inc}}(\mathbf{x})$, are the *scattered* and *incident* pressure fields in the exterior, $p^j(\mathbf{x})$ is the pressure field in Ω^j . For the sake of simplicity, the spatial variable \mathbf{x} will be dropped from now on.

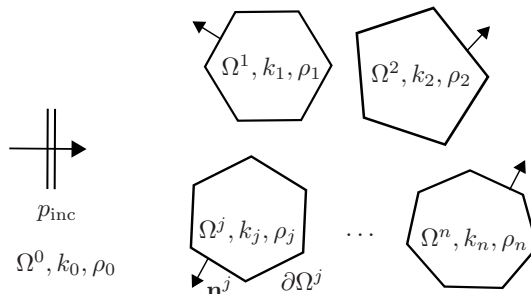


Figure 1: Schematic diagram of the multiple domains. Refer to the text for the details.

The last line in Eq. (1) is the Sommerfeld radiation condition that requires the scattered waves to be outgoing in the unbounded domain Ω^0 .

2.2. Coupled boundary integral formulation

The Calderón representation of the Helmholtz problem in the exterior domain Ω^0 is given by, see Appendix A for the derivations,

$$\left(\frac{1}{2}\text{Id} - \mathbf{A}_{k_0}\right) \gamma^+ p_{\text{tot}} = \gamma^+ p_s, \quad (3)$$

where $\gamma^+ := [\gamma_D^+ \ \gamma_N^+]^T$ is the exterior *Cauchy trace operator* at $\bigcup_{j=1}^n \partial\Omega^j$, Id is the identity operator, \mathbf{A}_{k_0} is the Calderón operator evaluated with the wavenumber of the exterior domain, $p_{\text{tot}} = p_{\text{inc}} + p_s$ is the total pressure in the exterior domain Ω^0 . Restricting the boundary integral operators to a single domain j results in

$$\begin{aligned} \left(\frac{1}{2}\text{Id} - \mathbf{A}_{k_0}^j\right) \gamma^{j,+} p_{\text{tot}} &= \sum_{i \neq j} \mathbf{A}_{k_0}^{ji} \gamma^{i,+} p_{\text{tot}} \\ &= \gamma^{j,+} p_s. \end{aligned} \quad (4)$$

Here, $\mathbf{A}_{k_0}^{ji}$ is the Calderón operator that takes the wavenumber k_0 and maps a surface potential at $\partial\Omega^i$ to $\partial\Omega^j$. The term $\sum_{i \neq j} \mathbf{A}_{k_0}^{ji} \gamma^{i,+} p_{\text{tot}}$ accounts for all cross scatterings between domains Ω^i and Ω^j for $i = 1, \dots, n$, $i \neq j$.

For the interior of domain Ω^j , the Calderón representation of the Helmholtz problem reads, see Appendix A for the derivations,

$$\left(\frac{1}{2}\text{Id} + \mathbf{A}_{k_j}^j\right) \gamma^{j,-} p^j = \gamma^{j,-} p^j, \quad (5)$$

where $\mathbf{A}_{k_j}^j$ is the Calderón operator evaluated in the interior of domain Ω^j .

The boundary conditions shown in Eq. (1) can be represented as follows

$$\gamma_D^{j,-} p^j = \gamma_D^{j,+} p_{\text{tot}}, \quad (6a)$$

$$\gamma_N^{j,-} p^j = \frac{\rho_j}{\rho_0} \gamma_N^{j,+} p_{\text{tot}}. \quad (6b)$$

Defining $D_j := \begin{bmatrix} \text{Id} & 0 \\ 0 & \rho_j/\rho_0 \end{bmatrix}$, Eq. (6) transforms to $\gamma^{j,-} p^j = D_j \gamma^{j,+} p_{\text{tot}}$. Substituting this relationship into Eq. (5) and multiplying both sides with D_j^{-1} produces

$$\left(\frac{1}{2}\text{Id} + \tilde{\mathbf{A}}_{k_j}^j\right) \gamma^{j,+} p_{\text{tot}} = \gamma^{j,+} p_{\text{tot}}, \quad (7)$$

where $\tilde{\mathbf{A}}_{k_j}^j := D_j^{-1} \mathbf{A}_{k_j}^j D_j$.

Subtracting Eq. (4) from Eq. (7) produces

$$\begin{aligned} & \left(\mathbf{A}_{k_0}^j + \tilde{\mathbf{A}}_{k_j}^j\right) \gamma^{j,+} p_{\text{tot}} + \sum_{i \neq j} \mathbf{A}_{k_0}^{j,i} \gamma^{i,+} p_{\text{tot}} \\ & = \gamma^{j,+} p_{\text{tot}} - \gamma^{j,+} p_s, \end{aligned} \quad (8)$$

which rearranges to the final form of the formulation as follows

$$\begin{aligned} & \left(\mathbf{A}_{k_0}^j + \tilde{\mathbf{A}}_{k_j}^j\right) \gamma^{j,+} p_{\text{tot}} + \sum_{i \neq j} \mathbf{A}_{k_0}^{j,i} \gamma^{i,+} p_{\text{tot}} \\ & = \gamma^{j,+} p_{\text{inc}} \quad \forall j = 1, \dots, n. \end{aligned} \quad (9)$$

This equation is called the Poggio-Miller-Chan-Harrington-Wu-Tsai (PMCHWT) formulation for the multiple domain HTP. This represents a set of linear equations which can be condensed into a block system $\hat{\mathbf{A}}_k \mathbf{u} = \mathbf{b}$ where

$$\hat{\mathbf{A}}_k := \left[\hat{\mathbf{A}}_k\right]_{ji} = \begin{cases} \mathbf{A}_{k_0}^j + \tilde{\mathbf{A}}_{k_j}^j & j = i \\ \mathbf{A}_{k_0}^{j,i} & j \neq i \end{cases}, \quad (10)$$

and

$$\mathbf{u}_j = \gamma^{j,+} p_{\text{tot}}, \quad \mathbf{b}_j = \gamma^{j,+} p_{\text{inc}}. \quad (11)$$

In the above equations the Calderón operator is a 2×2 block matrix represented by

$$\mathbf{A}_{k_j}^j := \begin{bmatrix} -\mathbf{K}^j & \mathbf{V}^j \\ \mathbf{W}^j & \mathbf{K}'^j \end{bmatrix}, \quad (12)$$

where \mathbf{V}^j , \mathbf{K}^j , \mathbf{K}'^j , \mathbf{W}^j are the single layer, double layer, adjoint double layer, and hypersingular boundary integral operators, respectively, see Appendix A for their definitions. Thus, $4n(n+1)$ boundary integral operators should be evaluated to construct the PMCHWT formulation for the HTP for n domains.

2.3. Operator preconditioning

The Galerkin method is used for the discretisation of boundary integral operators. The boundary $\partial\Omega^j$ is meshed by triangular elements. The discrete formulation results in a linear system of equations which corresponds to the matrix problem $\mathbf{A}\mathbf{u} = \mathbf{b}$ where

$$[\mathbf{A}]_{rq} = \langle \widehat{\mathbf{A}}_k \eta_q, \eta_r \rangle, \quad \forall q, r = 1, 2, \dots, z \quad (13)$$

$\mathbf{u} = [u_1, u_2, \dots, u_z]$ is the vector of unknown solution of the variational problem and $\mathbf{b} = [b_1, b_2, \dots, b_z]$ with

$$b_r = \langle \gamma^{j,+} p_{\text{inc}}, \eta_r \rangle. \quad (14)$$

Here, z is the number of degrees of freedom (dofs), η_q and η_r are the trial and test functions, and $\langle \cdot, \cdot \rangle$ is the standard L^2 dual pairing. The test and basis functions are linear piecewise continuous functions on the triangular surface mesh. The reader is referred to (Śmigaj, Betcke, Arridge, Phillips and Schweiger, 2015, Betcke et al., 2017) for further details.

This linear discrete system of equations is usually ill-conditioned at high driving frequencies and acoustic impedance mismatch between the exterior and interior domains. Consequently, iterative solvers such as GMRES converge very slowly. Hence, to improve the convergence rate of the iterative solvers. the preconditioned continuous problem $\mathbf{C}^{-1} \widehat{\mathbf{A}}_k \mathbf{u} = \mathbf{C}^{-1} \mathbf{b}$ is solved instead where the operator \mathbf{C} is defined such that the spectral condition number of the preconditioned system is smaller than the original system. The operator preconditioners are designed using the mapping properties of the BIE operators – instead of the discretised matrix – which allows them to be easily combined with acceleration and compression algorithms (Hiptmair, 2006, Kirby, 2010).

The performance of conventional operator preconditioners of PMCHWT formulation substantially deteriorates in scenarios with large wavenumbers (Antoine and Darbas, 2016) and high contrast domains (Gossye et al., 2018). Such scenarios are common in

HIFU treatment planning applications. Therefore, a new block-diagonal preconditioner was developed to regularise the PMCHWT equations for the multiple domain Helmholtz transmission problem. This new preconditioner is based on the Neumann-to-Dirichlet, denoted by Λ_{NtD} , and Dirichlet-to-Neumann maps, Λ_{DtN} . Λ_{NtD} maps the normal gradient of the pressure field on the boundary $\partial\Omega^j$ to the pressure field on the surface. Λ_{DtN} performs the inverse map. These maps evaluated in the exterior domain satisfy the following relationships (Antoine, Xavier and Darbas, Marion, 2007, Darbas et al., 2013)

$$\begin{aligned}\Lambda_{\text{DtN}}^{j,+} \mathbf{V}^{j,+} &= -\frac{1}{2}\mathbf{I} + \mathbf{K}'^{j,+}, \\ \Lambda_{\text{NtD}}^{j,+} \mathbf{W}^{j,+} &= -\frac{1}{2}\mathbf{I} - \mathbf{K}^{j,+}.\end{aligned}\tag{15}$$

The double layer and adjoint double layer operators are compact and therefore $\Lambda_{\text{DtN}}^{j,+} \mathbf{V}^{j,+}$ and $\Lambda_{\text{NtD}}^{j,+} \mathbf{W}^{j,+}$ are better conditioned than single layer and hypersingular operators. Thus, the DtN and NtD maps are used to build the following block diagonal preconditioner

$$\mathbf{C}^{-1} := [\mathbf{C}]_{ji} = \begin{cases} \mathbf{C}^j & j = i \\ 0 & j \neq i \end{cases},\tag{16}$$

where

$$\mathbf{C}^j := \begin{bmatrix} \Lambda_{\text{DtN}}^{j,+} & \\ & \Lambda_{\text{NtD}}^{j,+} \end{bmatrix}.\tag{17}$$

The preconditioner is designed with information of the self-interaction of the domains only. This is because the conditioning of $\widehat{\mathbf{A}}_k$ is mainly influenced by the diagonal blocks rather than cross-interactions between domains (the off-diagonal blocks).

In order to use this preconditioner with the PMCHWT formulation, the Calderón operators should be vertically permuted to place the hypersingular and single layer operators on the main diagonal. To preserve the RHS of Eq. (9), the blocks of the unknown vector $\mathbf{u}_j = \left[\gamma_D^{j,+} p_{\text{tot}} \quad \gamma_N^{j,+} p_{\text{tot}} \right]^T$ are permuted as well.

To implement this preconditioner, we need to calculate the DtN and NtD maps. These are non-local pseudo-differential operators with no closed-form solutions. However, an accurate approximation based on the high frequency asymptotics of them can be achieved using the on-surface radiation condition (OSRC) method (Antoine et al., 1999, Antoine, 2008). The expressions of the NtD and DtN maps approximated by the OSRC approach are given by

$$\widetilde{\Lambda}_{\text{DtN}} = ik \sqrt{1 + \frac{\Delta_{\Gamma}}{k_{\epsilon}^2}}, \quad (18a)$$

$$\widetilde{\Lambda}_{\text{NtD}} = \frac{1}{ik} \left(1 + \frac{\Delta_{\Gamma}}{k_{\epsilon}^2} \right)^{-1/2}. \quad (18b)$$

where $k_{\epsilon} = k + i\epsilon$ where $\epsilon > 0$ is a damped wavenumber and Δ_{Γ} denotes the Laplace-Beltrami operator. The singularities are avoided by using the damped wavenumber. A good choice of damping is $\epsilon = 0.4k^{-1/3}R_{\epsilon}^{-2/3}$ with R_{ϵ} the radius of the scatterer. The square root operations in above equations are approximated with a Padé series expansion with N_{Pade} terms. The reader is referred to (van 't Wout et al., 2015, Betcke et al., 2017, Darbas et al., 2013) for the details. Since the OSRC approximations of the NtD and DtN maps, Eqs. (18a) and (18b), are used to compute the elements of the preconditioner Eq. (16), it will be referred to as the OSRC block diagonal preconditioner. It should be noted that this block diagonal OSRC preconditioner is sparse which results in fast computation.

3. Numerical experiments

The number of surface elements required by BEM to represent the wave propagation is of $\mathcal{O}(k^2)$ which results in the memory footprint of $\mathcal{O}(k^4)$, as Galerkin discretisation of the boundary integral operators results in dense matrices. This prohibits the implementation of this BEM formulation for HIFU treatment planning on a typical computational platform. To alleviate this problem, the hierarchical matrix compression with the tolerance set to 10^{-6} is used to assemble the discretised boundary integral operators in a compressed format. Refer to (van 't Wout et al., 2015, Betcke et al., 2017) for complementary information about hierarchical matrices and their application for solving Helmholtz problems.

A workstation with 32 processors (Intel[®] Xeon(R) CPU E5-2683 v4@2.10 GHz) and 512 GB RAM was used for performing the following numerical experiments. First, the preconditioned formulation and its implementation was validated against analytical solutions for a model problem consisting of a spherical object in Section 3.1. Subsequently, the scattered field from i) human ribs and an abdominal fat layer, ii) a human kidney and a perinephric fat layer, exposed to the acoustic field generated by a HIFU array transducer is computed and discussed in Section 3.2.

The presented formulation was implemented in Python using the open source Bempp library (Śmigaj, Betcke, Arridge, Phillips and Schweiger, 2015), version 3.3.4. The GMRES algorithm of the SciPy library with the restart parameter set to 100 was used for solving the discrete system of equations. The GMRES scheme terminates when the relative residual is below a specified relative tolerance, which was set to 10^{-5} . The efficiency of the OSRC preconditioner Eq. (18) is affected by parameters R_{ϵ} and N_{Pade} . Although one can choose different R_{ϵ} and N_{Pade} for different domains, one set of values were selected to construct the preconditioner for the sake of simplicity. The larger N_{Pade} the more accurate the approximation of DtN and NtD maps are, but at the cost of more numerical operations at each iteration. The numerical investigations

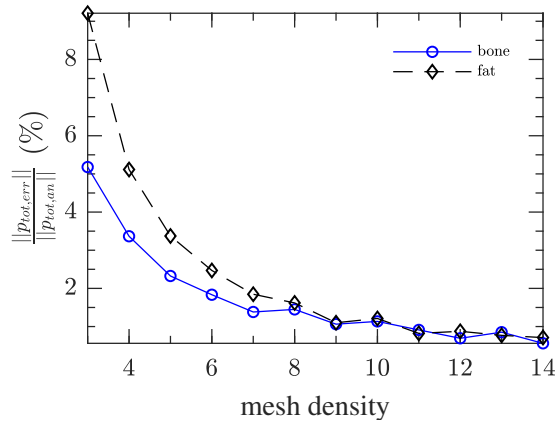


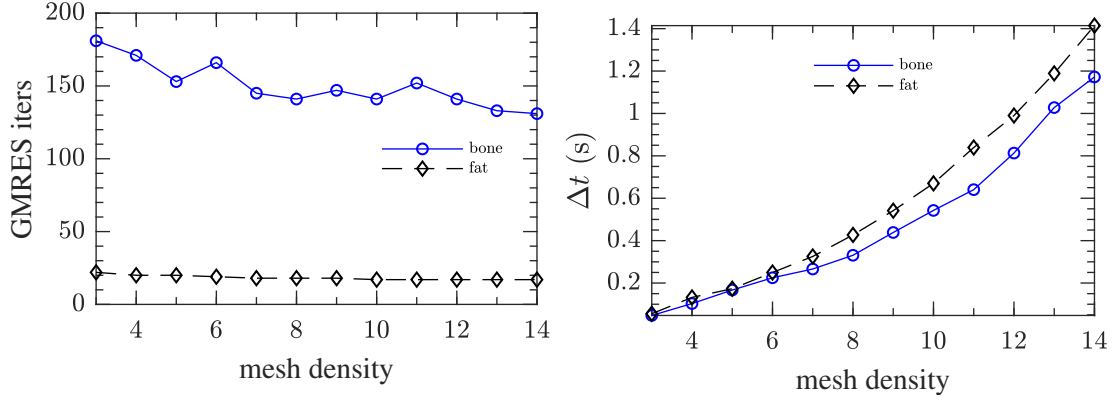
Figure 2: The percentage of the l_2 – norm of the difference between the computed total pressure by BEM and the analytical total pressure at different mesh densities.

demonstrate the following points: i) a relatively small size of Padé series, 4 for spheres and 8 for anatomical meshes, is sufficient to calculate the OSRC preconditioner and achieve expected performance, ii) setting R_ϵ to a value of one order of magnitude smaller than the characteristic size of the largest domain in the model leads to a fast convergence.

3.1. Single sphere model

The HTP problem of a single sphere object impinged by a plane wave is considered. The analytical solution is obtained using the classical series expansion method for a penetrable acoustic sphere (Anderson, 1950, Morse, 1968). The driving frequency is considered to be 1 MHz which is typically used in HIFU applications for the liver and kidney. The exterior medium is assumed to be water and the sphere possesses the physical properties of i) rib bones and ii) abdominal fat. The physical properties are listed in Table 1. The diameter of the sphere is 1 cm which is large enough to include multiple interior reflections at the wavelength of the sphere material, and which is of the order of magnitude of the anatomical heterogeneities considered in Section 3.2 of this paper. The problem was solved for a range of mesh densities, the latter parameter corresponding to the number of elements per wavelength associated with the material which has the smallest speed of sound. The value of $R_\epsilon = 5 \times 10^{-4}$ m is used for all the sphere simulations.

In order to compare BEM and analytical results, the l_2 – norm of the difference in the total pressure, $p_{\text{tot,err}} = p_{\text{tot}} - p_{\text{tot,an}}$ was calculated where p_{tot} is the computed pressure in the field by the BEM formulation and $p_{\text{tot,an}}$ is the analytical total pressure. The computational grid is a uniform 200×200 grid spanning from $-3R$ to $3R$, where R is the radius of the sphere, through the centre of the sphere. The predictions of the total field becomes more accurate, in the sense of l_2 – norm, as the mesh density increases, see Fig. 2. Nevertheless, with rather coarse surface meshes of 6 elements per wavelength, the error is below 3%. This choice permits the prediction of the total field relatively accurately and fast– the computation time per iteration (denoted by Δt) is



(a) Number of GMRES iterations at different mesh densities.

(b) The average GMRES time per iteration, i.e. Δt , at different mesh densities.

Figure 3: The convergence performance of the GMRES solver with tolerance 10^{-5} at different mesh densities. The mesh density is defined as the number of elements per wavelength.

about 0.2 s for both fat and bone spheres, see Figs. 3a and 3b. Bone is a high contrast material with $Z_{\text{int}}/Z_{\text{ext}} = 5.2$ where Z_{int} and Z_{ext} are the characteristic specific acoustic impedances of the interior and exterior domains. For such materials, making the surface mesh finer improves the convergence rate of the iterative solver, as shown in Figs. 3a and 3b. However, this comes at the expense of longer computation time per iteration because the matvec operations (the product of a matrix by a vector) of larger matrices need to be carried out. This improvement is negligible when the material contrast is small, i.e. fat with $Z_{\text{int}}/Z_{\text{ext}} = 0.86$.

3.2. Anatomical model problems

The results presented here are calculated for an incident field generated by a HIFU array transducer. The radius of the curvature of the array is 18 cm, the f-number is 1.18 and the focal point is located at the global origin by convention. The array features a pseudo-random spatial distribution of 256 piston elements, each of 6 mm diameter and facing towards the focal point. The details of calculating the HIFU incident field are presented in previous works, e.g. see (van 't Wout et al., 2015), and will not be repeated here.

The first anatomical example involves a clinically relevant scenario of targeting a tumour of the liver located at an intercostal space 3.5 cm behind ribs 10 and 11, on the right side, see Fig. 4. The scattering objects (domains) are i) an abdominal fat layer located in the vicinity of the anterior of the ribcage, and ii) two human ribs. These two domains are immersed in an infinite exterior domain possessing physical properties representative of the human liver. Ribs generally consist of a cancellous bone core enclosed by a shell of cortical bone, the thickness of which varies with gender and age. Examining micro CT scans of ribs, it is apparent that the majority of the volume of a rib

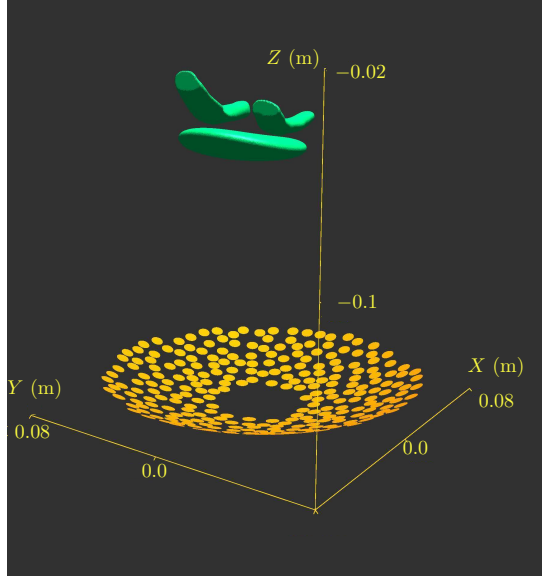
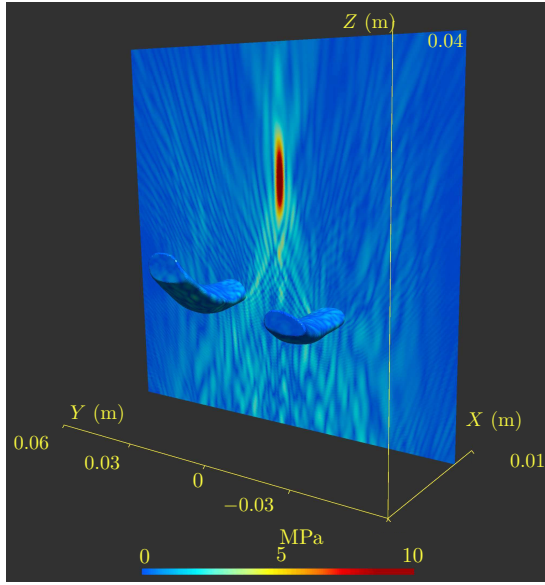


Figure 4: Schematic diagram of the HIFU array, the abdominal fat layer and the ribcage. The intersection of visualisation axes is $[-0.08,-0.08,-0.18]$.

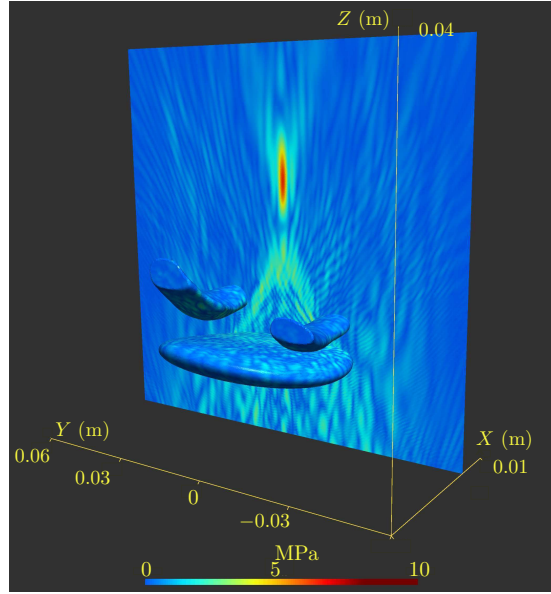
consists of cancellous bone (Perz et al., 2015, Holcombe et al., 2018). Thus, the physical properties of ribs used in the numerical simulations in this paper correspond to those of cancellous bone. The acoustic properties of all tissue media are listed in Table 1. The fat layer was assumed to possess an ellipsoidal cross section with a thickness of 10 mm close to the axis of the transducer. The distance between the surface of the fat layer and the ribs vary from 1 mm to 15 mm.

The surface meshes of domain j are made of triangles with an average element size of $\lambda/4$ where $\lambda = \min(\lambda_0, \lambda_j)$, $j = 1, 2$. This resulted in i) 44924 nodes (89848 dofs) in the fat domain, and ii) 30088 nodes (60176 dofs) in the ribs domain.

In the first instance, a simulation was carried out omitting the fat layer. The GMRES solver (with the same tolerance and restarts as before) solved the preconditioned equations for the ribs model in 74 iterations and 2 minutes. Adding the fat layer to the model increased the number of iterations to 82 and the runtime to just under 9 minutes. Here, $R_\epsilon = 10^{-4}$ m was used to calculate the OSRC preconditioner, Eq. (18). The computation of the discrete matrices with the standard \mathcal{H} -matrix compression technique took 80 and 465 minutes for the ribs only and fat and ribs problems, respectively. The simulation results are depicted in Figs. 5a to 6b. It can be observed that the presence of the fat layer leads to a drop in the peak pressure magnitude at the focus. Another interesting observation is the formation of a pre-focal high-pressure area caused by the constructive interference of the diffracted and transmitted waves through the fat layer. The significance of this observation and its clinical ramifications will however depend on the size, geometry and location of the fat layer with respect to the tumour and other tissue heterogeneities. The patient specificity of such features reinforces the need for

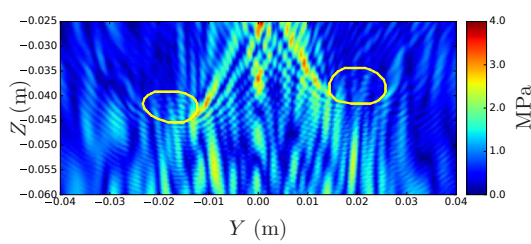


(a) Two ribs without a fat layer.

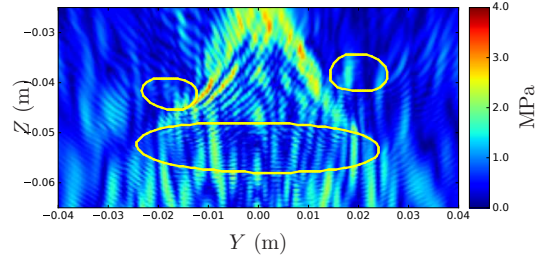


(b) Two ribs and a fat layer.

Figure 5: Calculated absolute value of p_{tot} for the case of two ribs (a) without a fat layer and (b) with a fat layer.



(a) Two ribs without a fat layer.



(b) Two ribs and a fat layer.

Figure 6: Calculated absolute value of p_{tot} at plane $Z = 0$, for the case of two ribs (a) without a fat layer and (b) with a fat layer. The colour bar limit was set to 4MPa for a better visualisation of the interior fields. Contours specify the boundary of the ribs and the fat layer.

treatment planning using validated numerical models, prior to a HIFU intervention, so that the potential impact of pre-focal heating may be gauged and subsequently mitigated. Figures 7a and 7b show the axial and lateral waveforms through the focus (i.e. along the Z and Y axes), respectively. The peak pressure at focus is reduced by almost 15% when accounting for transmission and scattering by ribs. Augmenting the model by including the fat layer, the peak pressure at focus decreases by about 50%.

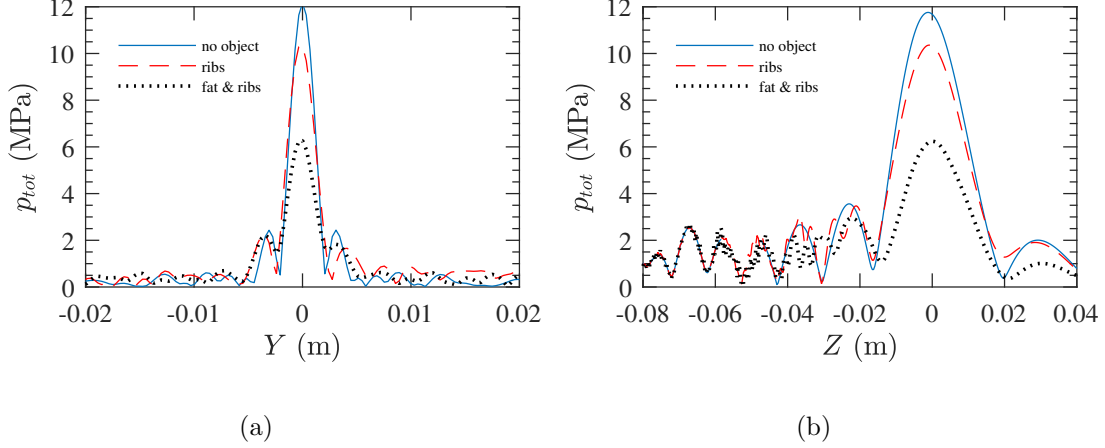


Figure 7: The absolute value of p_{tot} along (a) Y axis at $X = 0, Z = 0$, (b) along Z axis at $X = 0, Y = 0$.

The second anatomical example involves another clinically relevant scenario using HIFU to ablate a tumour of the kidney. The apex of the spherical section array is positioned at $[-0.13, 0.13, 0]$ m and the axis of transducer is colinear with the $[1, -1, 0]$ vector, thus resulting in the geometric focus of the array being inside the kidney. The scattering domains are i) a perinephric fat layer enclosing the kidney, and ii) a human kidney model. These two domains are immersed in an infinite exterior domain possessing physical properties of water. The physical properties of all domains are shown in Table 1. The thickness of the perinephric fat layer is about 10 mm and is placed 1 mm away from the kidney (constant gap).

Similar to the previous examples, the triangular surface meshes have an average element size of $\lambda/4$. The fat and kidney domains have 47766 and 65870 nodes (95532 and 131740 dofs), respectively. The R_ϵ parameter of the OSRC preconditioner was set to 10^{-3} m. The preconditioned equations were solved in 69 iterations which took about 35 minutes. Simulations are shown in Figs. 8a and 8b. Considering that the material contrasts in both domains are small, i.e. $Z_{fat}/Z_{water} = 0.86$ and $Z_{kidney}/Z_{water} = 1.10$, the aberration of the HIFU beam is negligible. This is better displayed in Fig. 9 which shows the magnitude of the axial pressure for different scenarios. The peak pressure at the focus is reduced by 15% due to the presence of the perinephric fat layer and the kidney. Eliminating the perinephric fat layer and keeping the kidney, the peak pressure at the focus only reduces by 5%. This problem was solved in 45 iterations and 12 minutes. The computation time to discretise and populate the matrix with \mathcal{H} -matrix compression is about 20 and 40 hours for the kidney only and kidney and perinephric fat models, respectively.

4. Conclusion

An innovative fast multiple-domain BEM formulation for solving the Helmholtz transmission problem was developed in this paper. The formulation uses a novel OSRC

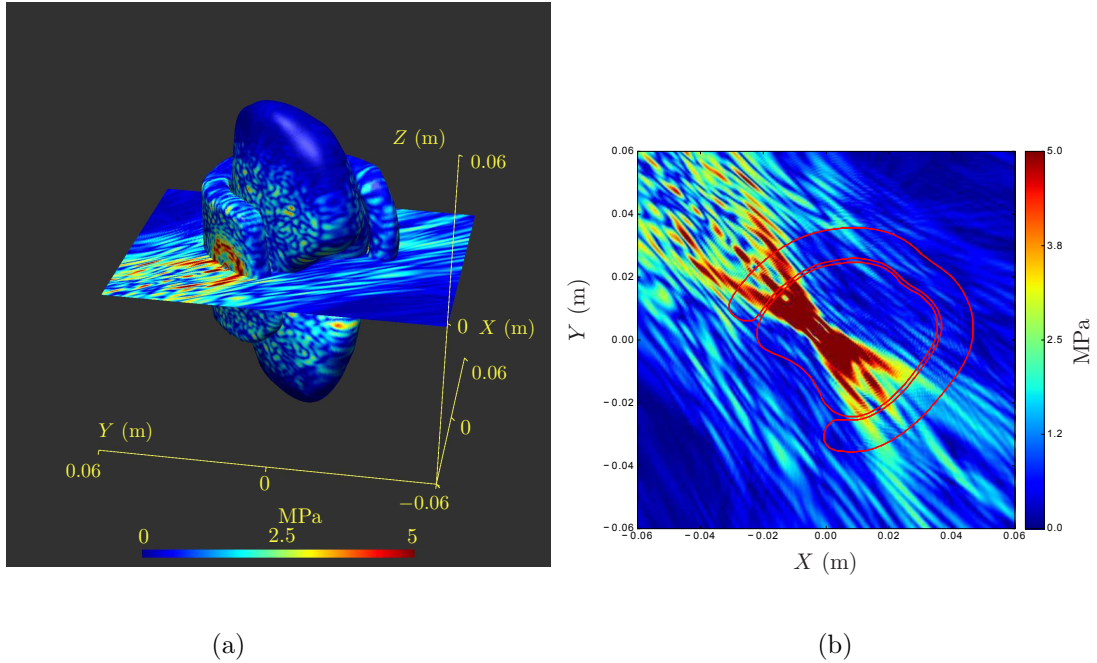


Figure 8: Calculated absolute value of p_{tot} for the case of a perinephric fat layer and the kidney: (a) in 3D, (b) at $Z = 0$ plane.

preconditioner and a variation of the multiple-domain PMCHWT. It was developed for HIFU treatment planning applications. The numerical simulations were performed to calculate the scattered field from i) a model of a human ribcage and an abdominal fat layer, and ii) a human kidney and perinephric fat layer, exposed to the acoustic field generated by a HIFU array transducer. The simulation results showed that the presence of tissue heterogeneities and strong scatterers such as bone can lead to substantial aberration of the focus, the formation of the pre-focal high-pressure area, and reduction in the peak pressure. The significance of these effects are patient specific which reinforces the need for treatment planning using validated numerical models prior to a HIFU intervention.

Furthermore, these results promote the application of the new OSRC block diagonal preconditioner and the multiple-domain BEM algorithm for fast and accurate patient-specific HIFU treatment planning for tumours of the abdomen. It was shown that the new preconditioner and formulation can still perform well when high contrast domains are present. Nevertheless, the computational performance of this solver can be further improved by speeding up the calculation of the Calderón operators. This will be the subject of our forthcoming paper.

Acknowledgments

This work was supported by the EPSRC [Grant No. EP/P012434/1] and CONICYT [FONDECYT No. 11160462].

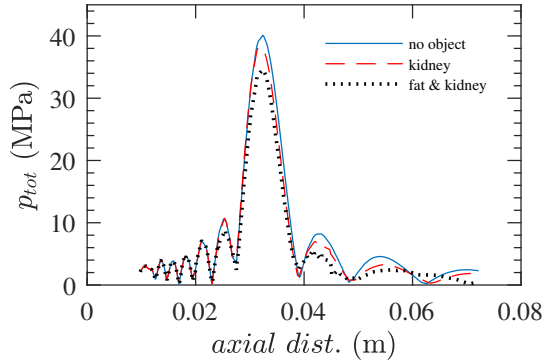


Figure 9: The absolute value of p_{tot} at $Z = 0$ plane along the axis of propagation, i.e. $[1, -1, 0]$ vector. The axial distances are determined from the centre of the array located at $[-0.13, -0.13, 0]$.

Table 1: Physical properties of the domains (Hasgall et al., 2018, Duck, 1990).

domain	ρ [kg m ⁻³]	c [m s ⁻¹]	α_0 [Np m ⁻¹ at 1 MHz]	b [DL]
ribs	1178	2117.5	47	1
fat	917	1412	9.3	1
kidney	1066	1554.3	2.8067	1
liver	1070	1640	7	1.30
water	1000	1500	0.015	2

Appendix A. Calderón operator

Solving the Helmholtz transmission problem with the BEM requires to reformulate the Helmholtz equation in the volume to boundary integral equations at the interfaces of two domains. This can be achieved by the aid of representation formulae which determine the acoustic fields from surface potentials at the boundaries. The representation formula for the domain j , ($j \neq 0$) reads

$$p^j = \text{SL}_{k_j}^j \psi^j(p^j) - \text{DL}_{k_j}^j \phi^j(p^j), \quad (\text{A.1})$$

where $\phi^j(p^j)$ and $\psi^j(p^j)$ are the jump potentials, and $\text{SL}_{k_j}^j$ and $\text{DL}_{k_j}^j$ are the single layer and double layer potential integral operators, respectively, and are given by

$$[\text{SL}^j \psi(p^j)](\mathbf{x}) = \int_{\partial\Omega^j} G_{k_j}(\mathbf{x}, \mathbf{y}) \psi(\mathbf{y}) d\Gamma(\mathbf{y})$$

$$\text{for } \mathbf{x} \notin \partial\Omega^j, \quad (\text{A.2})$$

$$[\text{DL}^j \phi(p^j)](\mathbf{x}) = \int_{\partial\Omega^j} \frac{\partial G_{k_j}(\mathbf{x}, \mathbf{y})}{\partial \mathbf{n}^j(\mathbf{y})} \phi(\mathbf{y}) d\Gamma(\mathbf{y})$$

for $\mathbf{x} \notin \partial\Omega^j$,

(A.3)

where $G_{k_j}(\mathbf{x}, \mathbf{y})$ denotes the Green's function for the Helmholtz equation given by

$$G_{k_j}(\mathbf{x}, \mathbf{y}) = \frac{e^{ik_j|\mathbf{x}-\mathbf{y}|}}{4\pi|\mathbf{x}-\mathbf{y}|}$$

for $\mathbf{x}, \mathbf{y} \in \Omega^j$ and $\mathbf{x} \neq \mathbf{y}$.

(A.4)

Taking the *Cauchy* trace, $\gamma^{j,\pm} := [\gamma_D^{j,\pm} \ \gamma_N^{j,\pm}]^T$, of the representation formula Eq. (A.1) produces

$$\begin{aligned} \gamma^{j,\pm} p^j &= \gamma^{j,\pm} \text{SL}_{k_j}^j(\psi^j(p^j)) - \\ &\gamma^{j,\pm} \text{DL}_{k_j}^j(\phi^j(p^j)) = \\ &\begin{bmatrix} \gamma_D^{j,\pm} \text{SL}_{k_j}^j(\psi^j(p^j)) - \gamma_D^{j,\pm} \text{DL}_{k_j}^j(\phi^j(p^j)) \\ \gamma_N^{j,\pm} \text{SL}_{k_j}^j(\psi^j(p^j)) - \gamma_N^{j,\pm} \text{DL}_{k_j}^j(\phi^j(p^j)) \end{bmatrix}. \end{aligned}$$
(A.5)

In order to further simplify this, we need to use the jump relations and their regularity across the boundary. The jump relations read

$$\begin{aligned} \gamma_D^{j,\pm} \text{SL}_{k_j}^j(\psi^j(p^j)) &= \mathbf{V}^j \psi^j(p^j), \\ \gamma_D^{j,\pm} \text{DL}_{k_j}^j(\phi^j(p^j)) &= \mathbf{K}^j \phi^j(p^j) \pm \frac{1}{2} \phi^j(p^j), \\ \gamma_N^{j,\pm} \text{SL}_{k_j}^j(\psi^j(p^j)) &= \mathbf{K}'^j \psi^j(p^j) \mp \frac{1}{2} \psi^j(p^j), \\ \gamma_N^{j,\pm} \text{DL}_{k_j}^j(\phi^j(p^j)) &= -\mathbf{W}^j \phi^j(p^j), \end{aligned}$$
(A.6)

where \mathbf{V}^j , \mathbf{K}^j , \mathbf{K}'^j , \mathbf{W}^j are the single layer, double layer, adjoint double layer, and hypersingular boundary integral operators defined as follows

$$[\mathbf{V}^j \psi(p^j)](\mathbf{x}) = \int_{\partial\Omega^j} G_{k_j}(\mathbf{x}, \mathbf{y}) \psi(\mathbf{y}) d\Gamma(\mathbf{y})$$

for $\mathbf{x} \in \partial\Omega^j$,

(A.7)

$$[\mathbf{K}^j \psi(p^j)](\mathbf{x}) = \int_{\partial\Omega^j} \frac{\partial G_{k_j}(\mathbf{x}, \mathbf{y})}{\partial \mathbf{n}^j(\mathbf{y})} \psi(\mathbf{y}) d\Gamma(\mathbf{y})$$

for $\mathbf{x} \in \partial\Omega^j$, (A.8)

$$[\mathbf{K}'^j \psi(p^j)](\mathbf{x}) = \frac{\partial}{\partial \mathbf{n}^j(\mathbf{x})} \int_{\partial\Omega^j} G_{k_j}(\mathbf{x}, \mathbf{y}) \psi(\mathbf{y}) d\Gamma(\mathbf{y}), \text{ for } \mathbf{x} \in \partial\Omega^j,$$
(A.9)

$$[\mathbf{W}^j \psi(p^j)](\mathbf{x}) = - \frac{\partial}{\partial \mathbf{n}^j(\mathbf{x})} \int_{\partial\Omega^j} \frac{\partial G_{k_j}(\mathbf{x}, \mathbf{y})}{\partial \mathbf{n}^j(\mathbf{y})} \psi(\mathbf{y}) d\Gamma(\mathbf{y})$$

for $\mathbf{x} \in \partial\Omega^j$. (A.10)

Inserting the jump relations into Eq. (A.5) results in

$$\begin{bmatrix} \mathbf{V}^j \psi^j(p^j) - \mathbf{K}^j \phi^j(p^j) \mp \frac{1}{2} \phi^j(p^j) \\ \mathbf{K}'^j \psi^j(p^j) \mp \frac{1}{2} \psi^j(p^j) + \mathbf{W}^j \phi^j(p^j) \end{bmatrix} = \begin{bmatrix} -\mathbf{K}^j \mp \frac{1}{2} \text{Id} & \mathbf{V}^j \\ \mathbf{W}^j & \mathbf{K}'^j \mp \frac{1}{2} \text{Id} \end{bmatrix} \begin{bmatrix} \phi^j(p^j) \\ \psi^j(p^j) \end{bmatrix},$$
(A.11)

which taking the identity matrix out gives the *Calderón operator* defined as follows

$$\mathbf{A}_{k_j}^j := \begin{bmatrix} -\mathbf{K}^j & \mathbf{V}^j \\ \mathbf{W}^j & \mathbf{K}'^j \end{bmatrix},$$
(A.12)

thus, Eq. (A.5) becomes

$$\gamma^{j,\pm} p^j = \left(\mp \frac{1}{2} \text{Id} + \mathbf{A}_{k_j}^j \right) \begin{bmatrix} \phi^j(p^j) \\ \psi^j(p^j) \end{bmatrix}.$$
(A.13)

For the PMCHWT formulation, the interior jump potentials read

$$\phi^j(p^j) = \gamma_D^{j,-} p^j,$$
(A.14a)

$$\psi^j(p^j) = \gamma_N^{j,-} p^j.$$
(A.14b)

Taking Eqs. (A.13) and (A.14) into consideration, the Calderón representation of the interior Helmholtz problem in domain Ω^j reads

$$\gamma^{j,-} p^j = \left(\frac{1}{2} \text{Id} + \mathbf{A}_{k_j}^j \right) \gamma^{j,-} p^j. \quad (\text{A.15})$$

With regards the exterior domain, we define the total scattered field in Ω^0 with p_s and the total exterior pressure as $p_{\text{tot}} = p_s + p_{\text{inc}}$. Incorporating these definitions, the exterior jump potentials for PMCHWT formulation become $\phi^0(p^0) = -\gamma_D^+ p_{\text{tot}}$ and $\psi^0(p^0) = -\gamma_N^+ p_{\text{tot}}$, and $\gamma^{0,+} p = \gamma^+ p_s$ where the *Cauchy* traces γ^+ are evaluated at $\bigcup_{j=1}^n \partial\Omega^j$. Substituting these equations into Eq. (A.13) yields the Calderón formulation of the exterior Helmholtz problem as follows, one should note that the Calderón boundary operator is evaluated with the exterior wavenumber k_0 ,

$$\gamma^+ p_s = \left(\frac{1}{2} \text{Id} - \mathbf{A}_{k_0} \right) \gamma^+ p_{\text{tot}}. \quad (\text{A.16})$$

References

- Anderson, V. C. (1950). Sound scattering from a fluid sphere, *The Journal of the Acoustical Society of America* **22**(4): 426–431.
- Antoine, X. (2008). Advances in the On-Surface Radiation Condition Method: Theory, Numerics and Applications, in F. Magoulès (ed.), *Computational Methods for Acoustics Problems*, Saxe-Coburg Publications, pp. 169–194.
- Antoine, X., Barucq, H. and Bendali, A. (1999). Bayliss-Turkel-like Radiation Conditions on Surfaces of Arbitrary Shape, *Journal of Mathematical Analysis and Applications* **229**(1): 184–211.
- Antoine, X. and Darbas, M. (2016). Integral Equations and Iterative Schemes for Acoustic Scattering Problems, in F. Magoulès (ed.), *Numerical Methods for Acoustics Problems*, Saxe-Coburg Editors.
- Antoine, Xavier and Darbas, Marion (2007). Generalized combined field integral equations for the iterative solution of the three-dimensional helmholtz equation, *ESAIM: M2AN* **41**(1): 147–167.
- Betcke, T., van 't Wout, E. and Gélât, P. (2017). *Computationally Efficient Boundary Element Methods for High-Frequency Helmholtz Problems in Unbounded Domains*, Springer International Publishing, pp. 215–243.
- Brunner, D., Junge, M., Rapp, P., Bebendorf, M. and Gaul, L. (2010). Comparison of the fast multipole method with hierarchical matrices for the helmholtz-bem, *Computer Modeling in Engineering & Sciences (CMES)* **58**(2): 131–160.
- Casper, A., Ballard, J. and Ebbini, E. (2010). Optimal transthoracic targeting of liver tumors using dual-mode ultrasound arrays: A numerical and experimental study, *AIP Conference Proceedings*, Vol. 1215, AIP, pp. 3–7.

- Cheng, C., Seybert, A. and Wu, T. (1991). A multidomain boundary element solution for silencer and muffler performance prediction, *Journal of Sound and Vibration* **151**(1): 119–129.
- Cranston, D. (2015). A review of high intensity focused ultrasound in relation to the treatment of renal tumours and other malignancies, *Ultrasonics sonochemistry* **27**: 654–658.
- Crocetti, L. (2018). Radiofrequency ablation versus resection for small hepatocellular carcinoma: Are randomized controlled trials still needed?
- Darbas, M., Darrigrand, E. and Lafranche, Y. (2013). Combining analytic preconditioner and fast multipole method for the 3-d helmholtz equation, *Journal of Computational Physics* **236**: 289 – 316.
- Duck, F. A. (1990). *Physical properties of tissue : a comprehensive reference book / Francis A. Duck.*, Academic Press, London.
- Duck, F. A. (2013). *Physical properties of tissues: a comprehensive reference book*, Academic press.
- Gélat, P., ter Haar, G. and Saffari, N. (2012). The optimization of acoustic fields for ablative therapies of tumours in the upper abdomen, *Physics in Medicine and Biology* **57**(24): 84718497.
- Gélat, P., ter Haar, G. and Saffari, N. (2014). A comparison of methods for focusing the field of a hifu array transducer through human ribs, *Physics in Medicine & Biology* **59**(12): 3139.
- Gossye, M., Huynen, M., Vande Ginste, D., De Zutter, D. and Rogier, H. (2018). A caldern preconditioner for high dielectric contrast media, *IEEE Transactions on Antennas and Propagation* **66**(2): 808–818.
- Hamilton, M. F., Blackstock, D. T. et al. (1998). *Nonlinear acoustics*, Vol. 237.
- Hasgall, P., Di Gennaro, F., Baumgartner, C. et al. (2018). IT'IS database for thermal and electromagnetic parameters of biological tissues v4.0.
- Hiptmair, R. (2006). Operator preconditioning, *Computers & Mathematics with Applications* **52**(5): 699–706.
- Holcombe, S. A., Hwang, E., Derstine, B. A. and Wang, S. C. (2018). Measuring rib cortical bone thickness and cross section from ct, *Medical Image Analysis* **49**: 27 – 34.
- Huang, S. and Liu, Y. (2016). A new simple multidomain fast multipole boundary element method, *Computational Mechanics* **58**(3): 533–548.
- Kirby, R. C. (2010). From functional analysis to iterative methods, *SIAM review* **52**(2): 269–293.
- Marburg, S. (2018). A pollution effect in the boundary element method for acoustic problems, *Journal of theoretical and computational acoustics* **26**(02): 1850018.
- Medeiros, A., Macarios, T., Azevedo, G. and Gardner, B. (2014). Predicting transmission loss of mufflers with perforated tube elements using the boundary element method, *Technical report*, SAE Technical Paper.
- Meloni, M. F., Chiang, J., Laeseke, P. F., Dietrich, C. F., Sannino, A., Solbiati, M., Nocerino, E., Brace, C. L. and Lee Jr, F. T. (2017). Microwave ablation in primary

- and secondary liver tumours: technical and clinical approaches, *International Journal of Hyperthermia* **33**(1): 15–24.
- Morse, P. M. P. M. (1968). *Theoretical acoustics*, International series in pure and applied physics, McGraw Hill, New York.
- Perz, R., Toczyski, J. and Subit, D. (2015). Variation in the human ribs geometrical properties and mechanical response based on x-ray computed tomography images resolution, *Journal of the Mechanical Behavior of Biomedical Materials* **41**: 292 – 301.
- Ramaekers, P., Ries, M., Moonen, C. T. and de Greef, M. (2017). Improved intercostal hifu ablation using a phased array transducer based on fermat’s spiral and voronoi tessellation: A numerical evaluation, *Medical physics* **44**(3): 1071–1088.
- Ritchie, R., Collin, J., Coussios, C. and Leslie, T. (2013). Attenuation and de-focusing during high-intensity focused ultrasound therapy through peri-nephric fat, *Ultrasound in medicine & biology* **39**(10): 1785–1793.
- Robertson, J. L., Cox, B. T. and Treeby, B. E. (2014). Quantifying numerical errors in the simulation of transcranial ultrasound using pseudospectral methods, *2014 IEEE International Ultrasonics Symposium*, pp. 2000–2003.
- Sartori, S., Di Vece, F., Ermili, F. and Tombesi, P. (2017). Laser ablation of liver tumors: An ancillary technique, or an alternative to radiofrequency and microwave?, *World journal of radiology* **9**(3): 91.
- ΩŚmigaj et al.
- Śmigaj, W., Betcke, T., Arridge, S., Phillips, J. and Schweiger, M. (2015). Solving boundary integral problems with bem++, *ACM Transactions on mathematical software* **41**(2): 6:1–6:40.
- Suomi, V., Jaros, J., Treeby, B. and Cleveland, R. O. (2018). Full modeling of high-intensity focused ultrasound and thermal heating in the kidney using realistic patient models, *IEEE Transactions on Biomedical Engineering* **65**(5): 969–979.
- ter Haar, G. (2007). Therapeutic applications of ultrasound, *Progress in biophysics and molecular biology* **93**(1-3): 111–129.
- van ’t Wout, E., Gélat, P., Betcke, T. and Arridge, S. (2015). A fast boundary element method for the scattering analysis of high-intensity focused ultrasound, *The Journal of the Acoustical Society of America* **138**(5): 2726–2737.
- Waked, I., Berhane, S., Toyoda, H., Chan, S. L., Stern, N., Palmer, D., Tada, T., Yeo, W., Mo, F., Bettinger, D. et al. (2017). Transarterial chemo-embolisation of hepatocellular carcinoma: impact of liver function and vascular invasion, *British journal of cancer* **116**(4): 448.
- Werner, J. D., Tregnago, A. C., Netto, G. J., Frangakis, C. and Georgiades, C. S. (2018). Single 15-min protocol yields the same cryoablation size and margin as the conventional 10–8–10-min protocol: Results of kidney and liver swine experiment, *Cardiovascular and interventional radiology* **41**(7): 1089–1094.
- Wu, H., Liu, Y. and Jiang, W. (2012). A fast multipole boundary element method for 3d multi-domain acoustic scattering problems based on the burton–miller formulation, *Engineering Analysis with Boundary Elements* **36**(5): 779–788.

Yuldashev, P. V., Shmeleva, S. M., Ilyin, S. A., Sapozhnikov, O. A., Gavrilov, L. R. and Khokhlova, V. A. (2013). The role of acoustic nonlinearity in tissue heating behind a rib cage using a high-intensity focused ultrasound phased array, *Physics in Medicine & Biology* **58**(8): 2537.